Optical probing of anisotropic heat transport in the quantum spin ladder Ca9La5Cu24O41

Otter, M.; Athanasopoulos, G.; Hlubek, N.; Montagnese, M.; Labois, M.; Fishman, D. A.; de Haan, Foppe; Singh, S.; Lakehal, D.; Giapintzakis, J.

Published in:
International Journal of Heat and Mass Transfer

DOI:
10.1016/j.ijheatmasstransfer.2012.01.007

Publication date:
2012

International Journal of Heat and Mass Transfer 55 (2012) 2531–2538

Contents lists available at SciVerse ScienceDirect

International Journal of Heat and Mass Transfer

journal homepage: www.elsevier.com/locate/ijhmt

Optical probing of anisotropic heat transport in the quantum spin ladder $Ca_9La_5Cu_{24}O_{41}$

M. Otter [a], G. Athanasopoulos [b], N. Hlubek [c], M. Montagnese [a], M. Labois [d], D.A. Fishman [a], F. de Haan [a], S. Singh [e], D. Lakehal [d], J. Giapintzakis [b], C. Hess [c], A. Revcolevschi [e], P.H.M. van Loosdrecht [a,*]

[a] Zernike Institute for Advanced Materials, Rijksuniversiteit Groningen, Nijenborgh 4, 9747 AG, The Netherlands
[b] Mechanical and Manufacturing Engineering, University of Cyprus, 75 Kallipoleos Avenue, P.O. Box 20537, Nicosia 1678, Cyprus
[c] IFW-Dresden, Institute for Solid State Research, P.O. Box 270116, D-01171 Dresden, Germany
[d] ASCOMP GmbH, Technoparkstr. 1, CH-8005 Zürich, Switzerland
[e] Laboratoire de Physico-Chimie de L'Etat Solide, ICMMO, UMR8182, Université Paris-Sud, 91405 Orsay CEDEX, France

ARTICLE INFO

Article history:
Received 17 August 2011
Received in revised form 12 December 2011
Accepted 12 December 2011
Available online 31 January 2012

Keywords:
Magnetic excitations
Quantum spin systems
Spin ladder
Anisotropic heat diffusion
Thermal imaging

ABSTRACT

A transient thermal imaging technique is used to monitor heat diffusion at the surface of the antiferromagnetic spin ladder material $Ca_9La_5Cu_{24}O_{41}$. This material shows highly anisotropic thermal conductivity due to a large uni-directional magnetic heat transport along the ladders. The thermal conductivity is measured using optical heating as well as electrical heating, yielding 37 ± 3 W m^{-1} K^{-1} for the fast (ladder) direction and 2.5 ± 0.5 W m^{-1} K^{-1} for the slow direction, respectively. The fast direction result is in agreement with the thermal conductivity measured using other dynamic methods, but about 60% lower than the thermal conductivity measured using steady state methods.

1. Introduction

One of the main problems in microelectronics is overheating. Microprocessors or Central Processing Units can produce heat fluxes as high as 2.5 MW m^2 [1]. Furthermore, due to miniaturization, the power production per unit area in computer systems increases up to 28% annually [2], and there is no sign of breaking this trend. Therefore, there is an increasing need for advanced cooling techniques, such as heat channelling [3,4], i.e. ideally one-dimensional conduction of heat away from sensitive components. Up to now, conventional solutions have employed micro tube arrays drilled in the heat sink and micro pumps to convey and control the flow of a suitable cooling fluid. This method, albeit being quite flexible, requires a rather elaborate manufacturing process in order to be both efficient and miniaturizable. For this reason, one would like to employ a bulk material with an inherently anisotropic, quasi one-dimensional heat conductivity. Moreover, a low (i.e. insulator like) electric conductivity would be desirable to allow an intimate contact with microelectronic compounds, while avoiding issues of current leakage and short circuits.

A class of materials that fulfills these conditions are the so-called low-dimensional quantum magnets $(Sr,Ca,La)_{14}Cu_{24}O_{41}$ [5–12], a family of copper oxide one-dimensional antiferromagnets that shows an important magnetic contribution to the heat conduction. In this class of cuprates, the copper oxygen layers are formed by the in plane stacking of two types of Cu–O linear structures (parallel to the crystal *c*-axis), which, considering the Cu spin structure and weak interaction between neighbouring structures, can be regarded as good realizations of the 1D spin chain and the quasi-1D spin ladder models. Since in the chain structure the copper atoms have vanishing spin, they do not contribute to heat transport. On the other side, in the Cu_2O_3 two-leg ladders the Cu $3d^9$ ions have spins $s = 1/2$ and are antiferromagnetically coupled via Cu–O–Cu superexchange interactions. The heat transport by the gapped spin excitations (magnons) is responsible for an anomalous anisotropic contribution to the heat conductivity along the *c*-axis; it dwarfs, even at room temperature, the isotropic lattice conductivity which remains dominant in the directions perpendicular to the *c*-axis. Along the *c*-axis a high variety between static and dynamic measurements is expected to be seen when going to timescales smaller than the thermalization time between magnons and phonons [13].

The compound with the highest anisotropy in thermal conductivity at room temperature, and therefore the most promising for

* Corresponding author.
E-mail address: P.H.M.van.Loosdrecht@rug.nl (P.H.M. van Loosdrecht).

0017-9310/$ - see front matter © 2012 Elsevier Ltd. All rights reserved.
doi:10.1016/j.ijheatmasstransfer.2012.01.007

Nomenclature

c_p	specific heat, J K^{-1} m^{-3}
D	diffusivity tensor, m^2 s^{-1}
G	Green's function, t^{-1}
s	spin
S	heating rate source, K s^{-1}
r	position, m
t	time, s
t_0	initial time, s
T	temperature, K
T_0	initial temperature, K
V	voltage, V
ΔT_0	initial temperature difference, K
ΔT	temperature difference, K

Greek symbols

κ	thermal conductivity, W K^{-1} m^{-2}
ρ	molar density, m^{-3}
σ	standard deviation, μm
v	(x,y) in-plane directions, m

Subscripts

$\parallel$	parallel to the surface
$\perp$	perpendicular to the surface
m	first measurement after heating pulse

applications, is the spin ladder $Ca_9La_5Cu_{24}O_{41}$ [6]. From neutron scattering and optical experiments a spin gap as large as 35 meV between the singlet ground state and the triplet excited state was found [14–16]. Such a high gap value, together with a large mean free path makes the magnon thermal conductivity ($\kappa_\parallel$) peak at high temperature, leading to a high thermal conductivity parallel to the spin structure at room temperature; $\kappa_\parallel$ is 95 W m^{-1} K^{-1}, i.e. a value comparable to that of nickel [6]. The ratio between the thermal conductivity $\kappa_\parallel$ (parallel to the c-axis) and $\kappa_\perp$ (perpendicular to the c-axis) is as high as 40 at room temperature. Since the cuprate compounds are Mott insulators they provide an escape route from the apparent paradox of having both a high thermal conductivity and an electrically insulating behavior in a metal oxide. Also, doping with switchable magnetic defects potentially makes tuning of the thermal conductivity possible.

In order to investigate the application of low-dimensional quantum magnets to thermal management of microelectronics, the experimental method employed should reproduce the thermal footprint of actual miniaturized electronic devices. Also, the ensuing thermal evolution has to be probed in a time-resolved fashion in order to measure the spatial and temporal thermal response of the device. The standard four-probe steady state method employed so far [17] for studying bulk heat conductivity in the compounds investigated here requires a uniform, constant heat current to allow reliable measurements and has certain limitations concerning sample size and shape. In the work described here the front surface of the sample is heated optically, using a laser pulse, or electrically, using deposited gold strips. The laser pulse is used to create a hot spot at the sample surface, while the gold strip on top of the sample resembles a microelectronic device consisting of a heat producing structure with a cooling substrate attached. Time-resolved fluorescent microthermal imaging (FMI) [18–20] is used to probe the time- and position-resolved temperature profile by detecting variations in the fluorescence intensity of a thin rare-earth chelate layer deposited onto the sample [21]. Distinctive advantages of this non-conventional optical technique arise when compared to the steady state method, such as the possibility to vary the heating volume and power and the short measurement time, combined with a broad applicability, ranging from thin films to the observation of heat transport patterns on real micro-chips and small electronic devices [19,20].

2. Experimental procedure

2.1. Sample preparation

The design and dimensions of the cross structure on the ac-plane of a $Ca_9La_5Cu_{24}O_{41}$ crystal, as well as the direction of the strips with respect to the crystal axis, are shown in Fig. 1. The $Ca_9La_5Cu_{24}O_{41}$ single crystal was grown by the travelling solvent floating zone method [22]. A thin platelet with the b-axis out of plane was cut from the crystal rod, giving a crystal surface parallel to the c-axis (magnon plus phonon transport) and the a-axis (only phonon transport). The surface was machine polished by SiC paper (5 μm grains) and subsequently by a cloth with 1 μm diamond suspension. The surface roughness was measured by a confocal microscope. By careful polishing, the surface RMS roughness was brought down to 20 nm. The gold structure was deposited by DC magnetron sputtering of Au thin films through a shadow mask on the polished ac-plane of the sample. The shadow mask is made out of hard, electroformed, sulphamate nickel. It is 50 μm thick and thinned to 5 μm thickness around the apertures in order to avoid problems during metal deposition associated with the mean free path of the metal ions, which has to be large enough for the ions to be able to pass across the entire thickness of the mask. A shadow mask was used in order to avoid the chemical treatment of the surface used in photolithography. Gold was chosen for the fabrication of the cross since it is not susceptible to oxidation. Because of its poor adhesion to oxides, a thin pre-layer of chromium was used as an adhesion promoter. The width of the strips was designed to be 10–12 μm, which was optimal for the 10 times magnification

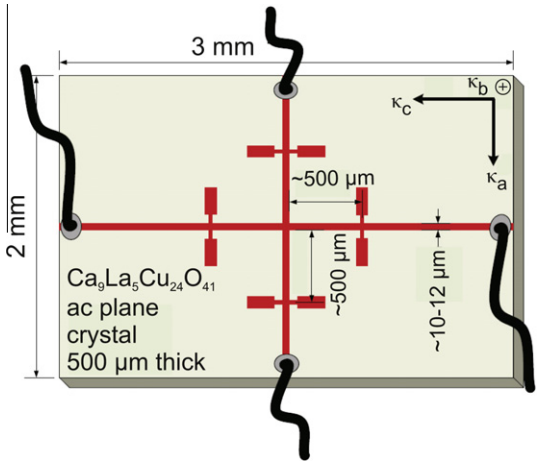

Fig. 1. Schematic picture of the gold cross (red/dark grey) deposited on the ac surface (light grey) of the $Ca_9La_5Cu_{24}O_{41}$ crystal. The dimensions of the cross and the sample are indicated. The thermal conductivities along the crystallographic axes a, b, c are indicated by κ_a, κ_b and κ_c, respectively. (For interpretation of the references to colour in this figure legend, the reader is referred to the web version of this article.)

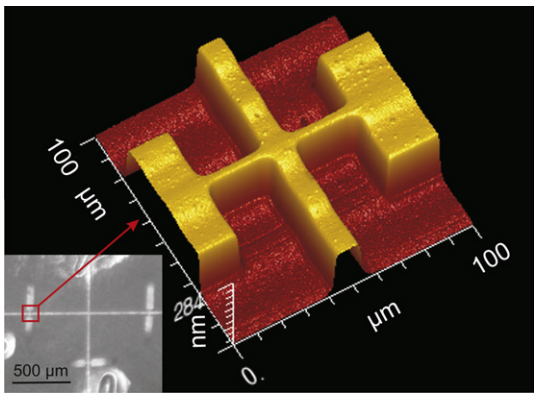

Fig. 2. 3D profile, measured by an optical profiler, of a detail of the deposited chromium/gold structure, showing well-defined lines. The inset shows a stereomicroscope photo of the sample. The red square indicates the part of the sample whose profile is shown. (For interpretation of the references to colour in this figure legend, the reader is referred to the web version of this article.)

objective of the microscope. The typical resistance between two end points of the cross was 100 Ω.

Fig. 2 shows a 3D profile of a deposited chromium/gold part of the cross structure, showing well-defined lines. The inset shows a stereomicroscope photo of the sample. The red circle indicates the part of the sample whose profile is shown. The thickness of the deposited chromium and gold cross is ~30 nm and ~100 nm, respectively, and its width, measured by an optical profiler and a scanning electron microscope (SEM), was ~12 µm. The metal lines were inspected for defects using both an optical microscope and an optical profilometer. After the deposition of the metal line, wire leads were connected to the pads. Wire bonding, a technique used during packaging of microelectronic devices, could not be employed due to the very thin metal layers (~130 nm) that prevent wire bonder's adhesion. Instead, silver paste was used to connect 25 µm gold wires to the sample pads. The sample was mounted on a dual-in-line ceramic package, as shown in Fig. 3.

2.2. Experimental setup

Following the procedure proposed by Kolodner and Tyson [20], a solution of 3 wt.% deuterated poly (methyl methacrylate) (dPMMA) and 2 wt.% rare-earth chelate europium thenoyltrifluoroacetonate (EuTTA, Acros Organics) in chlorobenzene was prepared and spincoated onto the samples, resulting in a thin (~400 nm) layer of EuTTA/dPMMA on the back side of the platelets. An optical excitation of TTA molecules in a wide band around 345 nm results in intersystem crossing and energy transfer to the Eu^{3+} ions, populating the f and d levels. Finally, the Eu^{3+} ions emit at several wavelengths corresponding to transitions from their f and d levels, which is strongest at 612 nm (Eu^{3+} 5d level) [23]. The overall quantum efficiency of the EuTTA layer photoluminescence decreases

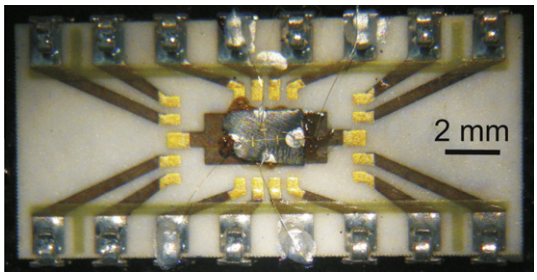

Fig. 3. Photograph of a dual-in-line ceramic package with the $Ca_9La_5Cu_{24}O_{41}$ single crystal, together with the deposited the gold structure and the wire contacts, mounted on it.

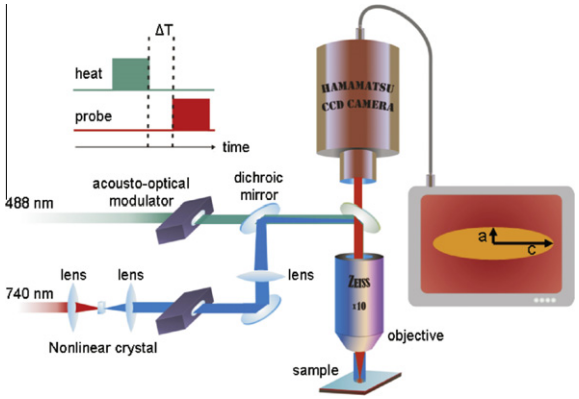

Fig. 4. Setup for the fluorescent microthermal imaging experiments. The optical heating experiment is depicted. In the electrical heating experiment two perpendicular gold strips on the surface are heated. For more details, see text.

monotonically with temperature in the interval from 273 to 330 K, as a result of thermal activation of non-radiative decay processes from the emitting Eu^{3+} 5d level (612 nm) to the Eu^{3+} 7f manifold [24]. The efficiency decrease in this temperature range was found to be around 4.4% K^{-1}. This is approximately twice larger than that of a EuTTA/non-deuterated-PMMA layer.

The experimental setup is shown in Fig. 4. For detecting temperature differences, the EuTTA layer fluorescence intensity was imaged before and after the electrical or optical heating pulse. From the relative difference in intensity between the two images the spatially resolved temperature difference was obtained. In the optical heating experiment, a focused 488 nm Argon-ion CW laser beam (spot size ~40 µm FWHM, power ~20 mW) heated a small volume of the sample at a position were no gold was deposited. The EuTTA/dPMMA layer is transparent for this wavelength. An acousto-optical modulator (AOM) was used to produce the desired pulse duration. In the electrical heating experiment, the two perpendicular gold strips forming a cross structure were Joule heated, one at a time. All measurements were done at room temperature. For both heating methods, the area around the heat pulse was illuminated by a defocused, 370, pulsed laser beam (the second harmonic of a Ti:Sapphire laser, repetition rate 80 MHz, power on the sample ~1.5 mW) to excite the EuTTA/dPMMA layer. Pulse trains with the desired duration were produced by a second AOM. The photoluminescence was collected by an objective, notch-filtered from heating/excitation radiation, and imaged onto a Peltier-cooled CCD-camera. The magnification of the objective was 10 times, which for the present system corresponded to a resolution of 1.6 µm per CCD pixel. The measurements were performed in a pump–probe fashion. The sample was heated either by a 20 µs laser pulse or by a 50 µs voltage pulse ($V \sim 10$ V). After the heating was switched off, the surface was imaged with different delays between heating and imaging laser, with integration time 20 or 30 µs. For every delay between pump and probe 400 measurements were accumulated. The synchronisation between the two AOM's and the processing of the images from the CCD-camera was automated. The smallest time-resolution achieved is 20 µs, enabling us to follow the time-evolution of the anisotropic heat diffusion at the surface in different directions. From that, the diffusion constant along different directions can be determined by fitting the data with the heat equation as is described in the following section.

3. Diffusion model

The observed temperature dynamics can be described by the anisotropic three-dimensional heat diffusion equation

$$\frac{\partial T}{\partial t} = \nabla(\mathbf{D}\cdot\nabla)T + S(\mathbf{r},t), \tag{1}$$

where T is the temperature, S is a source term depending on time t and position $\mathbf{r}$, and $\mathbf{D}$ is the (diagonal) diffusivity tensor. Eq. (1) has been integrated numerically using both ad hoc written software and the commercially available software package TransAT developed by ASCOMP GmbH [25], and the thermal parameters data of Ca9La5-Cu24O41 [6,8,9].

However, Eq. (1) can be simplified by noting that the diffusion dynamics along the z axis can be factorized out and ignored, since it does not couple with the diffusion parallel to the surface. Moreover, if the temperature dependence of the thermal parameters (thermal conductivity and specific heat) in Eq. (1) can be neglected, then the anisotropic heat diffusion equation at the surface reduces to [26]:

$$\frac{\partial T}{\partial t} = \sum_{v=x,y} D_v \frac{\partial^2 T}{\partial v^2} + S(\mathbf{r},t). \tag{2}$$

Here $D_v = \frac{\kappa_v}{\rho c_p}$ is the diffusion constant in the $v = x, y$ direction, c_p is the molar heat capacity and ρ is the molar density. Eq. (2) can be solved analytically through the Green's function formalism. With open boundary conditions, the in plane Green's function of the problem results in a product of two Gaussians:

$$G(x-x', y-y') = \prod_{v=x,y} \frac{1}{2\sqrt{\pi D_v t}} \exp\left[-\frac{(v-v')^2}{4D_v t}\right]. \tag{3}$$

As said, the diffusion along the z direction (perpendicular to the surface) is neglected, since it does not influence the evolution of the profile width in the (x,y) plane (parallel to the surface). To find the solution for the experimental conditions used in this work, the Green's function has to be convolved with the initial conditions induced by the joule and the optical heating profiles, respectively:

(i) For the Joule heating experiment, a temperature profile coinciding with the heated gold strip, rectangular in section and 10 μm wide along one direction, and of infinite length along the perpendicular direction, heated with a constant power in time for 50 μs.
(ii) For the optical heating, a two-dimensional Gaussian with full width half maximum 40 μm in space, with constant power in time for 20 μs.

Both heating methods produce temperature profiles that after the excitation quickly converge to a Gaussian shape. Therefore, a Gaussian-shaped initial temperature profile has been used in both cases as initial conditions. By performing the convolution we obtain

$$\Delta T = \Delta T_0 \prod_{v=x,y} \sqrt{\frac{t_{0,v}}{t - t_{0,v}}} \exp\left[-\frac{(v-v')^2}{4D_v\cdot(t-t_{0,v})}\right]. \tag{4}$$

Here ΔT_0 is the maximum of the $t = 0$ temperature profile. For the Joule heating experiment, there is no temperature gradient in the direction parallel to the strip. Therefore only one direction is considered. From Eq. (4) the Gaussian width (or the full width at half maximum FWHM $= 2.355\sigma$) can be extracted:

$$\sigma_v = \sqrt{2D_v\cdot(t-t_{0,v})} \quad v = x, y. \tag{5}$$

Following a standard approach, the introduced timeshift $t_{0,v}$ (representing the time at which the heating pulse is applied) is not treated as an independent fitting parameter, but is a direct function of the diffusivity and the value of the first data point collected after the heating pulse has vanished. By applying Eq. (5) to this data point we get:

$$t_{0,v} = t_m - \frac{\sigma_{t_m}^2}{2D_v}, \tag{6}$$

where t_m is the time at which the first measurement after the heat pulse is performed (in our case 20 or 30 μs), σ_{tm} is the measured standard deviation at $t = t_m$. In this treatment, the value of $t_{0,v}$ depends on the diffusion constant along that specific direction. Eq. (5) can be used to directly extract the thermal conductivity from the best fit to the standard deviation evolution in time.

As mentioned, this model can be applied only if the temperature dependence of the thermal constants of the problem can be safely ignored. This seems to be a reasonable assumption, since under the present experimental conditions the maximum temperature rise induced in the material by either the laser or the Joule heating is evaluated to be $\Delta T_0 = 45$ K. Considering the temperature before the excitation to be $T_0 = 300$ K, ΔT_0 induces an initial 15% thermal conductivity decrease and a 5% specific heat increase, and therefore a 20% decrease of the diffusivity. After the heating pulse has vanished, the temperature and the thermal parameter

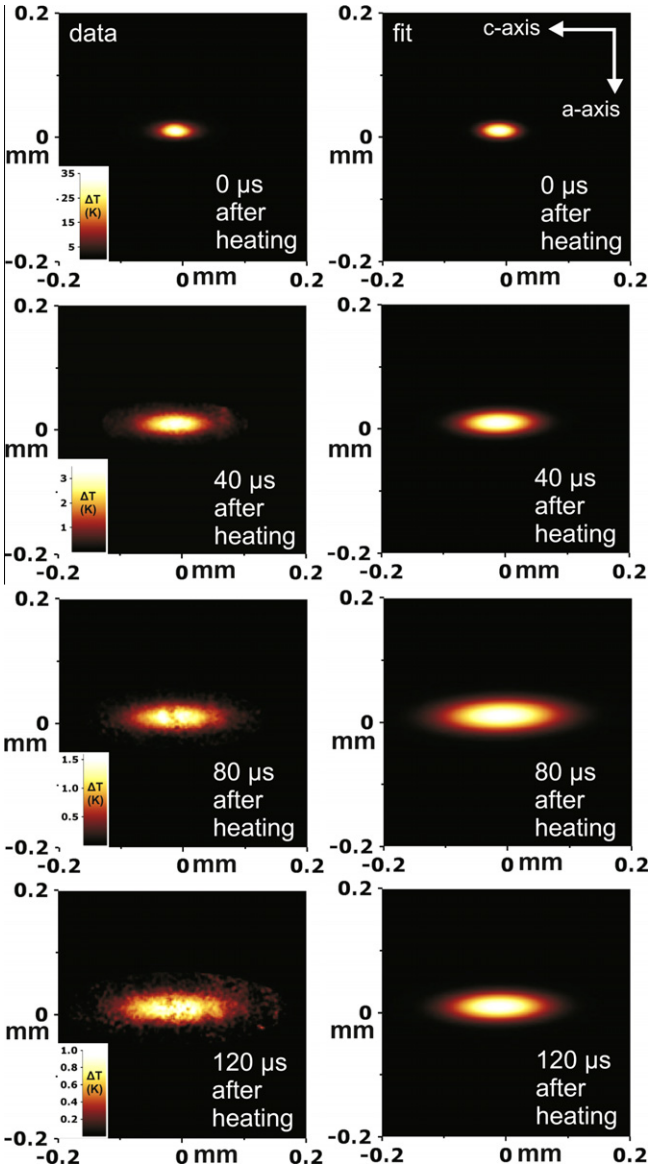

Fig. 5. Time evolution of the heat diffusion from a hot spot in the spin ladder compound $Ca_9La_5Cu_{24}O_{41}$. The left column shows the data, while the right column shows the best Gaussian fit to the data. Heating is done by a laser with a pulse duration of 20 μs. The integration time for the probe UV-pulse is 20 μs. The ladder direction is horizontal. The anisotropy of the diffusion process is clearly seen.

values relax back to their pristine values as $\Delta T \propto t^{-1}$ (see Eq. (4)). This assures that the maximum effect on the evolution of temperature profile widths would be less than 5% for most of the pump probe delays time considered here, i.e. well within the experimental uncertainties of the technique. This is also confirmed by comparing the solution to the one dimensional thermal diffusion model, where the thermal parameters have been fixed at their room temperature values, and a numerical solution of Eq. (1), where the full temperature dependence of the thermal parameters as reported in literature [6,8] is taken into account. Therefore, this simpler, analytical model will be used to fit and interpret the experimental results.

4. Results

4.1. Optical heating

In Fig. 5 the time evolution of the heat spread from a hot spot, created by a laser pulse, along the surface of the spin ladder compound $Ca_9La_5Cu_{24}O_{41}$ is shown for 4 different delay times between pump and probe beam. The left column shows the data, while the right column shows a 2-dimensional Gaussian fit to the data. Not all delay times are shown. In total, 10 delay times were measured, ranging from 0 to 180 μs, in steps of 20 μs. The temperature data are normalized in order to enhance the contrast at later times. The maximum temperature increase reached is 35 K. Fig. 6 shows the width of the fitted Gaussian as a function of delay time, extracted from the temperature profile parallel and perpendicular to the ladder. Fitting by the Gaussian one-dimensional model (Eq. (5)) is shown. The first datapoint is not considered in the fit because it is measured during the heating pulse. The thermal conductivities found are $\kappa_{\parallel} = 39 \pm 3$ W m^{-1} K^{-1} and $\kappa_{\perp} = 2.6 \pm 0.5$ W m^{-1} K^{-1}.

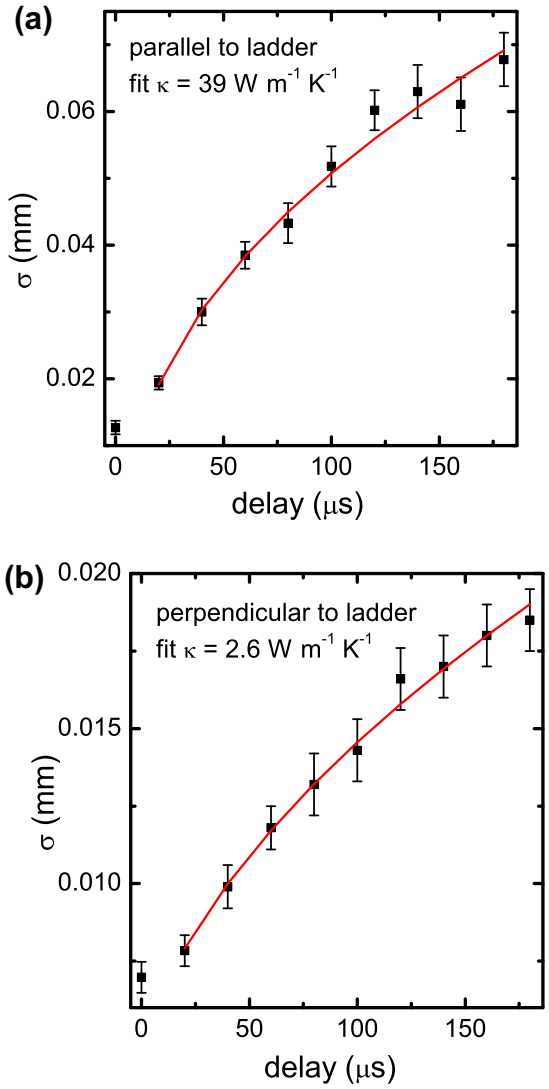

Fig. 6. Squares: standard deviation of the fitted Gaussian in Fig. 5 as a function of delay time extracted from the temperature profile of the heated surface. Line: fitting by the Gaussian one-dimensional model. (a) Direction parallel to the ladder. The thermal conductivity is $\kappa_{\parallel} = 39 \pm 3$ W m^{-1} K^{-1}. (b) Direction perpendicular to the ladder. The thermal conductivity is $\kappa_{\perp} = 2.6 \pm 0.5$ W m^{-1} K^{-1}.

4.2. Gold strip heating

Fig. 7 shows the time evolution of the heat spread from a hot gold strip, heated for 50 μs, along the surface of the spin ladder $Ca_9La_5Cu_{24}O_{41}$ single crystal for 5 different delay times between the heating and the probing pulse. In the left column, the data with the ladders perpendicular to the gold strip (parallel to the *x*-axis) are presented. In the right column, the data with the ladders parallel to the gold strip and the *y*-axis are presented. Not all delay times are shown. In total 12 delay times were measured, from 0 to 350 μs, in steps of 30 μs. The data are normalized in order to enhance the contrast at later times. The maximum temperature increase reached is 45 K. The evolution of the normalized

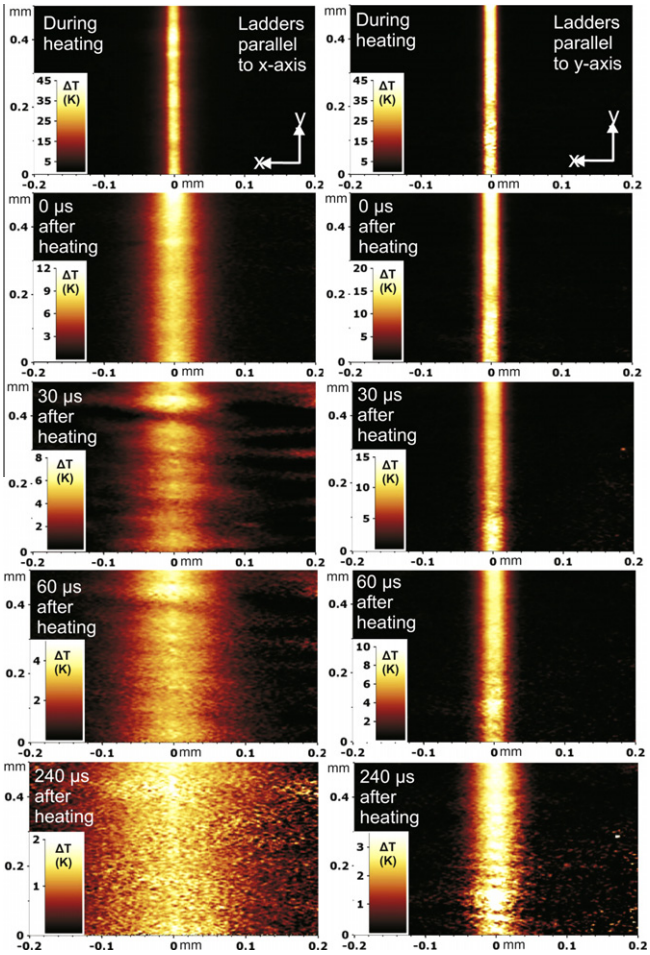

Fig. 7. Time evolution of the heat profile during and after electrically heating a hot gold strip for 50 μs in the spin ladder $Ca_9La_5Cu_{24}O_{41}$. The integration time for the probe UV-pulse is 30 μs. The ladder direction is horizontal for the images in the left column and vertical for the images in the right column. The anisotropy of the diffusion process is clearly seen.

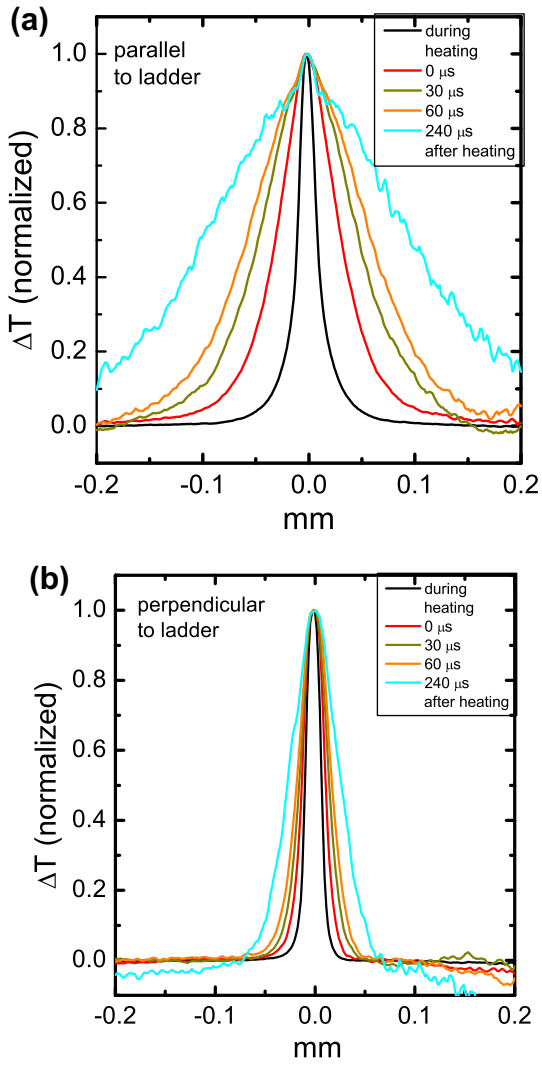

Fig. 8. Normalized temperature profiles parallel and perpendicular to the ladder for several delay times extracted from the left column of Fig. 7. The data are averaged over the *y*-direction.

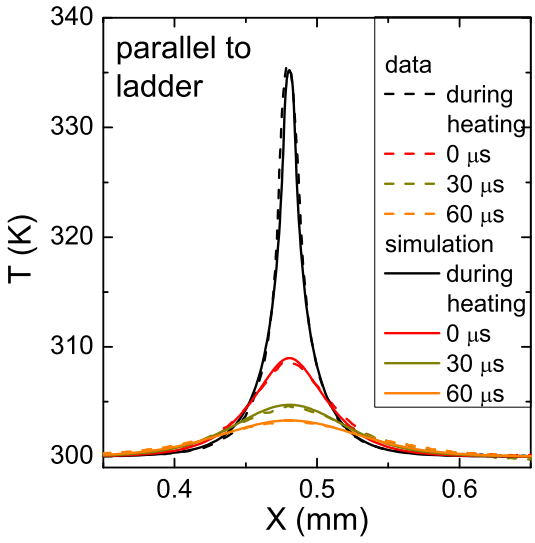

Fig. 9. Time evolution of the heat profile during and after electrically heating a hot gold strip for 50 μs in the spin ladder $Ca_9La_5Cu_{24}O_{41}$ parallel to the ladders. A comparison to a numerical simulation using TransAT software is shown, which is performed using a thermal conductivity parallel to the ladders of 34.5 W m^{-1} K^{-1}.

temperature profiles, averaged over the *y*-direction, are presented in Fig. 8 for diffusion parallel and perpendicular to the ladder direction. A simulation using TransAT software for this evolution is shown for the direction parallel to the ladders in Fig. 9. The initial conditions are a temperature of 300 K everywhere. The domain is $5 \times 5 \times 1$ mm, and the minimum cell size is 0.6 μm (ladder direction) by 12 μm (perpendicular to ladder direction) by 0.6 μm (out of plane direction). In total, there are $265 \times 100 \times 60$ cells. Time steps are 0.05 ms during heating and 0.01 ms after that. The thermal conductivity used parallel to the ladders is 34.5 W m^{-1} K^{-1} and perpendicular to the ladders 2.5 W m^{-1} K^{-1}. It is seen that the simulation reproduces the data quite well. From the time evolution data, the full width half maximum (FWHM) is extracted as a function of delay time, as shown in Fig. 10. This is fitted with the Gaussian one-dimensional model (Eq. (5)). The first datapoint is not considered in the fit, because it is measured during heating. The fitted thermal conductivities are $\kappa_{\parallel}$=34.5 ± 3 W m^{-1} K^{-1} and $\kappa_{\perp}$=2.3 ± 0.5 W m^{-1} K^{-1}, respectively. In order to test the influence of surface roughness, the optical heating experiment was repeated on another sample from the same batch which was polished down to a surface roughness of about 1 μm. For this sample, the thermal conductivity parallel to the ladders was about 40% lower than the value measured on the 20 nm RMS surface roughness, while perpendicular to the ladder it was about 60% lower, showing the role of surface scattering as a bottleneck for thermal diffusion at the surface. A possible explanation for the difference in measurements along surfaces with different roughness is the introduction of structural strain and/or static defects at the surface by polishing [29].

5. Discussion

The thermal conductivity of the $Ca_9La_5Cu_{24}O_{41}$ single crystal extracted from the present dynamic microthermal imaging experiment along the ladder is about 60% lower than the bulk value measured in a steady state experiment, which is 85 W m^{-1} K^{-1} for a crystal from the same rod. However, for different dynamic bulk experiments, a similar reduced value of $\kappa_{\parallel}$ has been reported; the dynamic methods used being the 3ω method [27] and the fluorescent flash method [28,21], which give a thermal conductivity between 40% and 60% lower than the static value. Since both surface and bulk measurements give comparable results, surface effects (defects or conduction by surface modes) cannot be invoked to explain the discrepancies observed, at least in the 20 nm RMS roughness samples.

These findings might be explained, presently at a qualitative level only, by considering: (i) that along the ladder direction heat is carried by interacting magnons and phonons (ii) that in all the experiments considered heat is injected through the phonons subsystem only; moreover the different thermometric methods used are all mainly sensible to the phonon temperature only. Therefore, the magnon contribution to the thermal conductivity is detected only if, during diffusion, phonons manage to thermally equilibrate – at least partially – with the magnetic subsystem. Therefore, the contribution to the total, measured thermal conductivity is maximum (vanishing) when the thermalization time is much shorter (longer) than the diffusion times considered. This model has been already proposed to explain, albeit in a quantitative fashion, the extreme variations in thermal conductivity found in some bulk antiferromagnetic materials [13]. Here, the diffusion dynamics considered takes place within few hundreds of microseconds; in this interpretative framework, this seems to hint to a rather long magnon–phonon thermalization time, in the order of few hundreds of microseconds. These findings, if confirmed, would allow

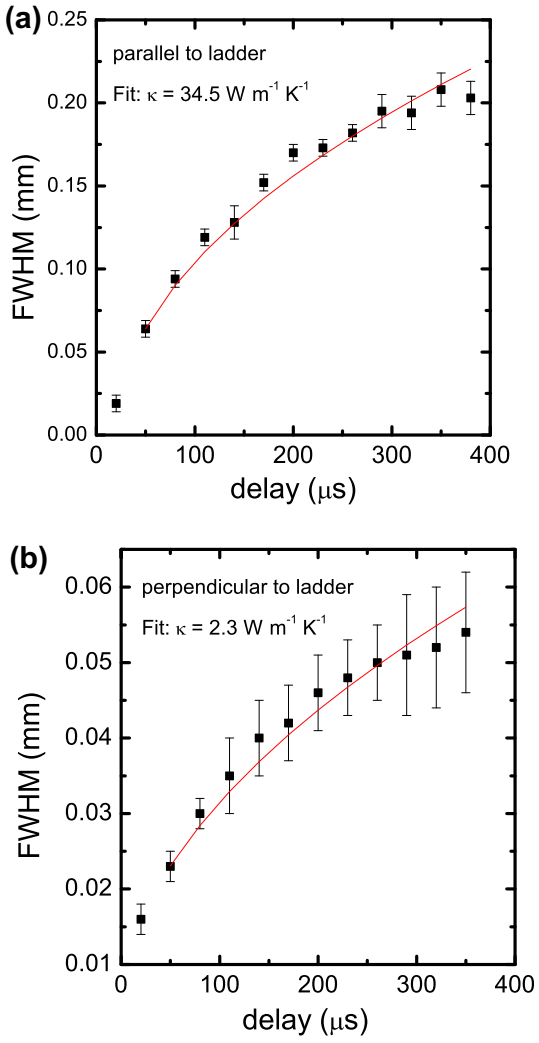

Fig. 10. Squares: full width half maximum (FWHM) as a function of delay time extracted from the temperature profile. Line: fitting by a one-dimensional model. Line: fitting by the one-dimensional model (Eq. (5)). (a) Direction parallel to the ladder. The thermal conductivity found is 34.5 ± 2 W m^{-1} K^{-1}. (b) Direction perpendicular to the ladder. The thermal conductivity found is 2.3 ± 0.2W m^{-1} K^{-1}.

to have access to the magnon–phonon thermalization dynamics by means of time resolved thermal transport measurements.

It has been pointed out that low dimensional quantum magnets can be promising candidates to improve the heat management in microelectronics, due to their electrically insulating behavior and highly anisotropic thermal conduction as measured by steady state methods [8]. If heat is applied by means of short (i.e. tens of microsecond) pulses, however, the thermal conductivity is measured to be between 40% and 60% lower than under steady state conditions. Therefore, if a high value of the thermal conductivity is the main criterion, the magnetic (i.e. highly anisotropic) heat transport channel is best effective for slowly varying heat sources. However, if a large anisotropy is the most critical parameter, then this material suits application as a directional heat transport channel for quickly varying heat sources as well, the dynamic anisotropy still being around 15.

6. Conclusion

In conclusion, a time-resolved thermal imaging technique has been used to monitor heat diffusion along the surface in different directions in the spin ladder material $Ca_9La_5Cu_{24}O_{41}$. This material shows a highly anisotropic bulk thermal conductivity due to large uni-directional magnetic heat transport along the ladder structure. The thermal conductivity is measured using optical heating as well as using electrical heating. The results of both methods are in good agreement; 37 ± 3 W m^{-1} K^{-1} for the fast direction parallel to the ladders and 2.5 ± 0.5 W m^{-1} K^{-1} for the slow direction perpendicular to the ladders, respectively. The thermal conductivities in the fast and slow direction, measured in a dynamic way, are in agreement with other dynamic measurements in the bulk material. However, in the fast direction the dynamic thermal conductivity is about 60% lower than the steady state value. The highly anisotropic heat transport properties of this material, both in the bulk and along the surface, can potentially be applied in directional cooling of microelectronics.

Acknowledgements

We thank Gert ten Brink for sample preparation and H.M.M.Hesp for technical assistance. This work was supported by the European Commission through the NOVMAG project (FP6-032980) and through the LOTHERM project (PITN-GA-2009-238475).

References

[1] R. Singh, A. Akbarzadeh, M. Mochizuki, Sintered porous heat sink for cooling of high-powered microprocessors for server applications, Int. J. Heat Mass Transfer 52 (9–10) (2009) 2289–2299.
[2] K.G. Brill, Heat density trends in data processing, computer systems, and telecommunications equipments: perspectives, implications, and the current reality in many data centers. White paper, The Uptime Institute Inc., version 2.0, New York, USA, 2006, (2005–2010), pp. 1–16.
[3] I. Mudawar, Assessment of high-heat-flux thermal management schemes, IEEE Trans. Components Packag. Tech. 24 (2) (2001) 122–141.
[4] S.V. Garimella, V. Singhal, Dong Liu, On-chip thermal management with microchannel heat sinks and integrated micropumps, in: Proceedings of the IEEE, vol. 94, no. 8, 2006, 1534–1548.
[5] T. Siegrist, L.F. Schneemeyer, S.A. Sunshine, J.V. Wazczak, R.S. Roth, A new layered cuprate structure-type, $(A_{1-x}\ A'_x)_{14}Cu_{24}O_{41}$, Mater. Res. Bulletin 23 (10) (1988) 1429.
[6] C. Hess, C. Baumann, B. Büchner, Scattering processes and magnon thermal conductivity in $La_5Ca_9Cu_{24}O_{41}$, J. Magn. Magn. Mater. 290–291 (2005) 322.
[7] C. Hess, P. Ribeiro, B. Büchner, H. ElHaes, G. Roth, U. Ammerahl, A. Revcolevschi, Magnon heat conductivity and mean free paths in two-leg spin ladders: a model-independent determination, Phys. Rev. B 73 (10) (2006) 104407.
[8] C. Hess, Heat conduction in low-dimensional quantum magnets, Euro. Phys. Rev. J. Special Topics 151 (1) (2007) 73–83.
[9] R. Shaviv, E.R. Westrum, T.L. Yang, C.B. Alcock, B. Li, Thermodynamics of the (lathanum + strontium + copper + oxygen) high t_c superconductors i. heat capacities of $srcuo_2$, sr_2cuo_3 and $sr_14cu_24o_41$, j. Chem. Thermodyn. 22 (11) (1990) 1025–1034.
[10] U. Ammerahl, B. Büchner, L. Colonescu, R. Gross, A. Revcolevschi, Interplay between magnetism, charge localization, and structure in $Sr_{14-x}Ca_xCu_{24}O_{41}$, Phys. Rev. B 62 (13) (2000) 8630.
[11] U. Ammerahl, B. Büchner, C. Kerpen, R. Gross, A. Revcolevschi, Ising-like antiferromagnetism in $Ca_9La_5Cu_{24}O_{41}$, Phys. Rev. B 62 (6) (2000) 3592.
[12] D. Mienert, H.H. Klauss, A. Bosse, D. Baabe, H. Luetkens, M. Birke, F.J. Litterst, B. Büchner, U. Ammerahl, A. Revcolevschi, A. Amato, U. Zimmermann, B. Hitti, S. Kreitzman, The interplay of charge order and magnetism in the one-dimensional quantum spin system $Sr_{14}Cu_{24}O_{41}$, Phys. B Condens. Matter 326 (1–4) (2003) 440–445.
[13] D.J. Sanders, D. Walton, Effect of magnon–phonon thermal relaxation on heat transport by magnons, Phys. Rev. B 15 (3) (1977) 1489.
[14] S. Notbohm, P. Ribeiro, B. Lake, D.A. Tennant, K.P. Schmidt, G.S. Uhrig, C. Hess, R. Klingeler, G. Behr, B. Büchner, M. Reehuis, R.I. Bewley, C.D. Frost, P. Manuel, R.S. Eccleston, One- and two-triplon spectra of a cuprate ladder, Phys. Rev. Lett. 98 (2) (2007) 027403.
[15] M. Windt, M. Grüninger, T. Nunner, C. Knetter, K.P. Schmidt, G.S. Uhrig, T. Kopp, A. Freimuth, U. Ammerahl, B. Büchner, A. Revcolevschi, Observation of two-magnon bound states in the two-leg ladders of $(Ca,La)_{14}Cu_{24}O_{41}$, Phys. Rev. Lett. 87 (12) (2001) 127002.
[16] E. Dagotto, Experiments on ladders reveal a complex interplay between a spin-gapped normal state and superconductivity, Rep. Prog. Phys. 62 (11) (1999) 1525.
[17] C. Hess, B. Büchner, U. Ammerahl, A. Revcolevschi, Phonon thermal conductivity in doped La_2CuO_4: relevant scattering mechanisms, Phys. Rev. B 68 (18) (2003) 184517.

[18] W.J. Parker, R.J. Jenkins, C.P. Butler, G.L. Abbott, Flash method of determining thermal diffusivity, heat capacity, and thermal conductivity, J. Appl. Phys. 32 (9) (1961) 1679.
[19] D.L. Barton, P. Tangyunyong, Fluorescent microthermal imaging – theory and methodology for achieving high thermal resolution images, Microelectron. Eng. 31 (1-4) (1996) 271–279.
[20] P. Kolodner, J.A. Tyson, Microscopic fluorescent imaging of surface temperature profiles with 0.01° c resolution, J. Appl. Phys. 40 (9) (1982) 782.
[21] M. Otter, V.V. Krasnikov, D.A. Fishman, M.S. Pshenichnikov, R. Saint-Martin, A. Revcolevschi, P.H.M. van Loosdrecht, He at transport imaging in the spin-ladder compound $Ca_9La_5Cu_{24}O_{41}$, J. Magn. Magn. Mater. 321 (7) (2008) 796.
[22] A. Revcolevschi, U. Ammerahl, G. Dhalenne, Crystal growth of pure and substituted low-dimensionality cuprates $CuGeO_3$, La_2CuO_4, $SrCuO_2$, Sr_2CuO_3 and $Sr_{14}Cu_{24}O_{41}$ by the floating zone and travelling solvent zone methods, J. Crys. Growth 198–199 (1999) 593–599.
[23] H. Winston, O.J. Marsh, C.K. Suzuki, C.L. Telk, Fluorescence of europium thenoyltrifluoroacetonate. I. Evaluation of laser treshold parameters, J. Chem. Phys. 39 (2) (1963) 267.
[24] J. Georges, J.M. Mermet, Simultaneous time-resolved fluorescence and thermal lens measurements: application to energy transfer studies in europium chelates, Spectrochim. Acta 49A (1993) 397.
[25] Transat: Equations & algorithms, transat handbook series 2.3.0, Ascomp gmbh, 2010. <www.ascomp.ch/transat>.
[26] H.S. Carlslaw, J.C. Jaeger, Conduction of Heat in Solids, Oxford University Press, Oxford (UK), 1959.
[27] G.I. Athanasopoulos, E. Svoukis, Z. Viskadourakis, J. Giapintzakis, in: Thermal Conductivity Measurements of Anisotropic Bulk Samples Using the 3ω Method, in: Daniela S. Gaal, Peter S. Gaal (Eds.), Thermal Conductivity 30/ Thermal Expansion, 18, DEStech Publications Inc., Lancaster, PA, 2010 (Chapter 4).
[28] M. Montagnese, M. Otter, N. Hlubek, R. Saint-Martin, S. Singh, A. Revcolevschi, C. Hess, P.H.M. van Loosdrecht, Optical time domain studies of magnetic heat transport in quantum spin chains and ladders: first evidence of magnon–phonon decoupling at the ms scale, unpublished results.
[29] Koshi Takenaka, Kenji Iida, Yuko Sawaki, Shunji Sugai, Yutaka Moritomo, Arao Nakamura, Optical reflectivity spectra measured on cleaved surfaces of $La_{1-x}Sr_xMnO_3$: evidence against extremely small drude weight, J. Phys. Soc. Jpn. 68 (6) (1999) 1828–1831.